Additive Manufacturing 91 (2024) 104338

Contents lists available at ScienceDirect

Additive Manufacturing

journal homepage: www.elsevier.com/locate/addma

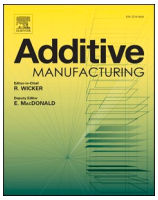

Laser powder bed fusion synthesis of nanoparticle reinforced CoCrFeNi

Vivek Devulapalli [a,*], Fiona Schulz [b], Erika Soares Barreto [c,d], Nils Ellendt [c,d], Eric A. Jägle [b], Gerhard Dehm [a,*]

[a] Max-Planck-Institut für Eisenforschung GmbH, Max-Planck-Str. 1, Düsseldorf DE-40237, Germany
[b] Institute of Materials Science, Universität der Bundeswehr München, Neubiberg DE-85579, Germany
[c] Leibniz-Institute for Materials Engineering – IWT, Badgasteiner Str. 3, Bremen DE-28359, Germany
[d] Faculty of Production Engineering, University of Bremen, Badgasteiner Str. 3, Bremen DE-28359, Germany

ARTICLE INFO

Keywords:
Additive manufacturing
Laser powder bed fusion
Compositionally complex alloys
High entropy alloys
Nanoparticle reinforcement
Dispersion strengthening

ABSTRACT

Nanoparticle reinforced metallic composites manufactured using laser powder bed fusion (LPBF) provide an economically viable avenue to obtain high strength near-net shaped critical components in automotive and aviation industry. In this study, the equiatomic compositionally complex alloy (CCA) CoCrFeNi is manufactured by LPBF with two types of reinforcing particles, titanium nitride (TiN) and titanium oxide (TiO_2). The reinforcing particles are introduced with varying size and volume concentration to the CCA powder fulfilling two purposes – improving the flowability of the feedstock and to cause nanoparticle strengthening, as demonstrated here using nanoindentation. We focus on the microstructure and texture evolution of all the alloys, and the phase transitioning of the particles. TiN nanoparticles of all sizes dissolve in the melt pool and uniformly precipitate as TiO_2. We observed distinctive core-shell nanoparticle formation with higher TiN content that also resulted in 45 % higher tensile strength. The successful integration of homogenously distributed nanoparticles without inducing cracks or defects and with superior mechanical properties signifies a leap forward in the fabrication of high-performance metal matrix composites like the commercial oxide dispersion strengthened (ODS) alloys.

1. Introduction

Compositionally complex alloys (CCAs), also known as medium- and high-entropy alloys (MEAs, HEAs) represent a new approach for alloy development that has been thoroughly researched in recent years due to their promising mechanical properties [1,2]. CoCrFeNi is a promising CCA known for its superior mechanical properties, particularly at cryogenic temperatures. Its low stacking fault energy helps to achieve superior ductility with high strength [3,4]. More recently, CoCrFeNi has been produced using laser powder bed fusion (LPBF), an additive manufacturing process that uses a laser beam to selectively melt metal powder to create near-net shape components. Studies have shown that LPBF produces CoCrFeNi with higher yield strengths and refined grain sizes than traditional manufacturing methods, indicating superior mechanical performance [5–7].

CCAs as the matrix for metal matrix composites (MMCs) have been the subject of several recent investigations. MMCs are a promising class of materials that offer a synergistic combination of the ductility of metals and the high strength and stiffness of ceramic reinforcements such as thermally stable carbides, nitrides, or oxides. Strengthening mechanisms that arise from the presence of hard reinforcing particles in a soft matrix is well understood [8,9]. The reinforcing particles that have higher stiffness than the matrix carry the applied load, similar to the continuous fiber reinforced composites, resulting in strengthening. The plastic strain due to residual thermal stress in the matrix around the particles increases the dislocation density by a few orders of magnitude, resulting in increased strain hardening. The size of the reinforcing particles can have a strong influence on resulting mechanical properties. While micron-sized (larger) particles can result in cracking at the particle-matrix interface, alloys reinforced with nanoparticles, even with a low volume fraction, exhibit remarkable improvement in fracture strength owing to reduced stress concentration and reduced particle cracking [10–12].

There are two main types of production processes for nanoparticle reinforced MMCs: in-situ and ex-situ. Ex-situ synthesis strategies involve incorporating the reinforcement into liquid or powdered metal, whereas

* Corresponding authors.
E-mail addresses: v.devulapalli@mpie.de (V. Devulapalli), fiona.schulz@unibw.de (F. Schulz), sbarreto@iwt.uni-bremen.de (E.S. Barreto), ellendt@iwt.uni-bremen.de (N. Ellendt), eric.jaegle@unibw.de (E.A. Jägle), g.dehm@mpie.de (G. Dehm).

https://doi.org/10.1016/j.addma.2024.104338
Received 22 March 2024; Received in revised form 21 July 2024; Accepted 2 August 2024
Available online 7 August 2024

in-situ procedures result in the processing-related reactions that produce nano-sized ceramic reinforced MMCs [13]. Achieving homogeneity in the particle dispersion is a frequent difficulty in the manufacturing of nanoparticle reinforced MMCs. This is especially true for commonly employed methods such as stir casting or powder sintering [14]. Mechanical stirring can result in porosity, gas phase nucleation on the particle surface that makes the nanoparticles float to the top of the melt and result in inhomogeneous distribution [10]. Ultrasonication during solidification can distribute and disperse nanoparticles in matrix with non-linear effects in liquids, especially transient cavitation [15]. In case of poor wettability, nanoparticles are more prone to a defective distribution due to their high surface area. Nanoparticles, due to their high surface area, are prone to poor wettability. Efforts to enhance matrix-reinforcement wettability, which subsequently reduce the nanoparticle agglomerates in conventional processing include methods like metallic coating, preheating particles, and adding reactive elements to the melt [13]. More recently, LPBF has been shown to be highly effective in obtaining a uniform particle dispersion in MMC [16,17]. Nanoparticles can be mixed to the powder feedstock to melt and uniformly precipitate in the alloy. For example, Chang et al. demonstrated that the addition of SiC to AlSi10Mg led to in-situ formation of uniformly dispersed Al4SiC4 [18]. Incorporating AlN into AlSi10Mg, Du et al. observed a transition from particle segregation to uniform dispersion in the alloy as the laser energy per unit length decreased from high (1800 J/m) to low (450 J/m) [19]. However, a systematic investigation of the influence of change in the added particle types and sizes for a given alloy remains unexplored.

The addition of particles to the powder feedstock can result in a change in the powder bed density, heat and mass transfer resulting from a change in laser absorptivity and the thermal profile under the laser beam [16]. Furthermore, some researchers have shown that the added nanoparticles can serve as grain refiners [20] and nucleation sites, allowing for the manufacturing of a variety of commercial alloys with a wide solidification temperature range. For example, the commercially important 7075 and 6061 series aluminum alloys were reinforced with hydrogen-stabilized zirconium particles to produce equiaxed grains and make them printable, that would otherwise have produced solidification defects [21,22]. The energy density obtainable in LPBF in combination with the high surface to volume ratio of nanoparticles allows ceramic nanoparticles with very high melting points like TiB_2 or TiC to melt [23]. Thermo-fluidic simulations reveal that Marangoni flow, driven by surface tension gradients from high temperature gradients in the melt pool, is crucial for the strong intermixing.

Oxygen, with its considerable anion radius that prevents it from being accommodated interstitially in solids, is a potent element that dissolves in molten pools. It reacts quickly with numerous metals at high temperatures and forms oxide precipitates upon cooling in the liquid metal. Oxides already present as inclusions in the powder feedstock can melt completely in melt pool and form a fine dispersion [24–28]. The role of inclusions in the enhancement of mechanical properties is heavily discussed [25–27,29]. In most cases, the nanoparticle/ oxide formation has been attributed to strengthening and improved fatigue life. The oxide precipitation has been observed to be restricted to the cellular boundaries, which are the regions where oxide forming elements also tend to segregate. This makes it harder to distinguish the strengthening contribution arising from the cell walls and the particles [30].

In a previous study, we investigated powder characteristics for LPBF through blending the atomized metal powder with the strengthening particles [31,32]. We found that nanoparticle mixing may improve the flowability. In this study, we use such powder blends with varying sizes and volume concentrations of titanium nitride (TiN) and titanium oxide (TiO_2) in LPBF to produce and explore matrix reinforced CoCrFeNi medium entropy alloys. In addition to the improved powder flowability, the reinforcing particles are expected to strongly influence the composite microstructure. In the following sections, we discuss the printing parameter window selection, the grain size and texture evolution, the particle size and its distribution and the phase transitions that the particles undergo.

2. Material and methods

2.1. Powder conditioning

The compositionally complex $Co_{25}Cr_{25}Fe_{25}Ni_{25}$ metallic powder was synthesized using close-coupled gas atomization under an Argon atmosphere and subsequently classified into size fractions ranging from 20 to 90 μm, as detailed by Gärtner et al. [31].

To create powder blends, reinforcing particles with varying compositions, sizes, and concentrations were added ex-situ to the gas-atomized base material. Two compositions were selected based on their distinct properties. The first consisted of nanosized Titanium nitride (TiN) particles with cubic structure and high purity (CAS No.: 25583–20–4, purity >99.2 %). Two commercially available sizes, 800 nm (US1023M) and 80 nm (US2260), both purchased from US Research Nanomaterials, Inc., were chosen for this study. The material has a melting point (T_m) of 3203 K and a density (ρ) of 5.22 g/cm^3.

For the second composition, rutile titanium dioxide (TiO_2) submicron powder (below 5 μm) was used, obtained from Sigma-Aldrich with high purity (CAS No.: 1317–80–2, purity ≥99.9 %). The TiO_2 powder has $T_m = 2116$ K and $\rho = 4.23$ g/cm^3.

Blends were prepared with 0.5 vol% particle additions for all three types of reinforced particles. Additionally, to enable comparison, a blend was prepared with a higher concentration of 5 vol% of 800 nm sized TiN. The powders were mixed using a three-dimensional shaker mixer (Turbula T2F, WAB GmbH) for 24 h at a rotational speed of 101 rpm, and Zetabeads 3.0 (Netzsch) grinding media of size fraction 2.6–3.3 mm was additionally employed to enhance the dry-coating over the bulk powder surface. Note that after 24 h of mixing, the powder exhibited improved flowability. For calculating the volume additions, we considered a density of 8.35 g/cm^3 for the medium-entropy $Co_{25}Cr_{25}Fe_{25}Ni_{25}$ alloy. To evaluate a suitable processing window for additively manufacturing high-quality, dense specimens (above 99 %) of reinforced CoCrFeNi, a total of 500 g of material was prepared for each powder batch.

Overall, five different materials including the CoCrFeNi reference were prepared, as displayed in Table 1. Representative scanning electron microscopy (SEM) images were acquired with a TESCAN VEGA II XLH are displayed in Fig. 1. EDS composition obtained from both the powder feed are tabulated in Sup. Table 1.

2.2. LPBF sample fabrication

Sample fabrication was carried out on a LPBF system (AconityMIDI+ or Aconity3D GmbH) equipped with a single-mode fiber laser (P_{max} = 700 W) featuring a nominal laser spot size of approximately 90 μm. To identify optimal parameters to achieve materials with high density, the processing window for each alloy variant was examined. The investigation involved varying the laser powers P from 150 to 350 W and the laser speeds v_s from 200 to 1000 mm/s. Throughout the process, a layer thickness d_s was maintained at 50 μm and a hatch distance (h) of 70 μm, with a bidirectional stripe pattern rotated 90° between layers as the

Table 1
Summary of the investigated powder blends.

Base alloy	Reinforcing particle	Size	Concentration	Sample name
$Co_{25}Cr_{25}Fe_{25}Ni_{25}$	-	-	-	Base alloy
	TiN	80 nm	0.5 vol%	TiN/0.5/80
	TiN	800 nm	0.5 vol%	TiN/0.5/800
	TiN	800 nm	5.0 vol%	TiN/5/800
	TiO_2	< 5 μm	0.5 vol%	TiO_2/0.5/<5000

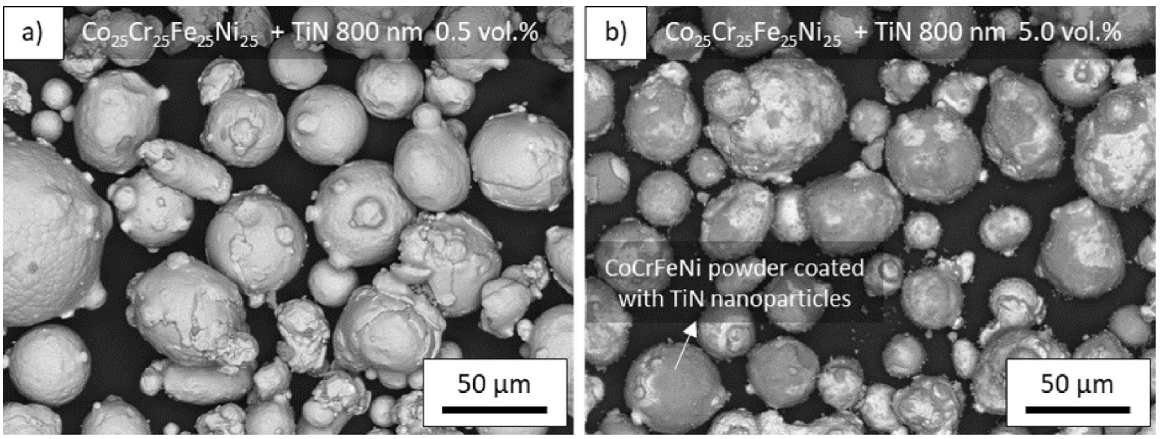

Fig. 1. SEM micrographs of $Co_{25}Cr_{25}Fe_{25}Ni_{25}$ powder dry-coated with a) 0.5 vol% and b) 5.0 vol% TiN particles of 800 nm size. Notably, in (b), the particles coated with TiN nanoparticles (as indicated) exhibit a discernibly darker contrast.

scanning strategy. In total, 25 cuboid specimens (4 × 4 × 10 mm^3, length × width × height) for each powder blend were additively manufactured under Argon atmosphere onto 316 L substrates (55 mm diameter). The residual oxygen content was maintained below 100 ppm during the entire process, as monitored by the integrated sensor of the machine. For comparative reasons, the LPBF process parameters were evaluated and summarized by the volume energy density E_v, commonly employed to describe the energy input per volume as a function of applied parameters:

$$E_V = \frac{P}{(v_s \bullet d_s \bullet h)} \quad \left[\frac{J}{mm^3}\right] \tag{1}$$

Regarding the porosity evaluation, microsections of the specimens were prepared by cross-sectioning along the build direction, and hot embedding in epoxy resin was conducted for subsequent grinding and polishing. The specific surface impacted by the gas and perpendicular to the powder feed (incoming from the left to the right direction) was selected for analysis. The resulting density percentage was determined through image analysis (PixelFerber) of optical micrographs (Stereomicroscope MZ16, Leica) of polished un-etched surfaces. Table 2 displays the volume energy density values achieved using different laser scanning parameters. The highlighted cell indicates the combination of scan speed and laser power that yielded the highest relative density. Fig. 2 illustrates the relative density resulting from variations in volume energy density for each investigated alloy variant. The dashed lines and the arrow point towards the region that typically resulted in highest density. The figure presents exemplary optical micrographs of specimens produced at varying volume energy density values, including suboptimal and excessive levels, along with a relatively dense specimen.

Based on this initial evaluation, it is evident that the highest relative densities were obtained with intermediate to low volume energy densities, in which values ranging from 100 to 125 J/mm^3 seem suitable for all investigated alloy compositions. Consequently, for subsequent sample production intended for microstructure investigation, a laser power of 300 W and a laser speed of 800 mm/s were employed, resulting in a volume energy density of approximately 107 J/mm^3.

Table 2
Parameter selection to evaluate LPBF process window to obtain dense and crack-free CoCrFeNi alloys.

Volume energy density (J/mm^3)		Laser power P (W)				
		150	200	250	300	300
Scan speed (mm/s)	200	214	286	357	429	500
	400	107	143	179	214	250
	600	71	95	119	143	167
	800	54	71	89	107	125
	1000	43	57	71	86	100

2.3. Material characterization

Printed cylindric samples were wire cut into thin 500 µm slices using electric discharge machining. Standard metallography techniques were employed for grinding and polishing. Electropolishing of the samples was conducted using a Struers Lectropol-5 apparatus with Struers A2 electrolyte, applying 17 V at room temperature for 20 s at a flow rate of 14. A dual beam SEM (Thermo Fisher Scientific Scios 2 HiVac) equipped with electron backscatter diffraction (EBSD) detector and a retractable STEM detector was utilized for secondary electron imaging, SEM-STEM imaging and EBSD analysis. A standard lift-out technique was utilized in the focused ion beam (FIB) with Ga+ -ion source to extract a transmission electron microscopy (TEM) lamella. The beam current was gradually reduced in several steps starting from 1 nA at 30 kV for coarse milling to eventually 27 pA at 2 kV for final polishing to obtain a thickness of < 100 nm. The scanning TEM (STEM) analysis including the imaging, energy dispersion spectroscopy (EDS), electron energy loss spectroscopy (EELS) and the nanobeam diffraction was performed in the Titan Themis 80–300 (Thermo Fischer Scientific). Python-based image analysis was performed on the HAADF-STEM images to measure the particle size and their area fraction. For TiN/5/800 samples with numerous cuboidal particles, we measured the area of the projected rectangles and calculated the diameter of a circle with equivalent area. On average, 100 particles per sample were measured for this analysis.

EDS signal was acquired using Thermo Scientific ChemiSTEM Super-X EDS detector. EELS signal was acquired using Gatan imaging filter (GIF Quantum ERS) spectrometer with a 5 mm entrance aperture. Zero-loss and core-loss EELS were simultaneously acquired using DualEELS option in Digital micrograph software. Dispersion of 0.5 eV/ch and collection angle of 16.1 mrad were utilized. Power law fit was used for the background correction and plural scattering due to sample thickness was considered for quantification. Hartree-Slater model provided with Digital Micrograph software was used for evaluating excitation cross-section. Exemplary background windows and edge models used for EELS quantification are shown in the Sup. Fig. 3.

We used nanoindentation to assess the influence of the nanoparticle addition on mechanical properties. Nanoindentation was performed in a G200 instrument (former Agilent, now KLA) to a maximum depth of 500 nm with a Berkovich diamond indenter. The continuous stiffness measurement (CSM) method was applied at a constant strain rate of 0.05 s^{-1} with a frequency of 45 Hz and harmonic displacement of 2 nm. We assumed Poisons ratio of 0.3 to calculate the elastic modulus.

Tensile tests were carried out on cylindrical specimens with a gauge length of 24.5 mm and a nominal diameter of 4 mm, machined from test

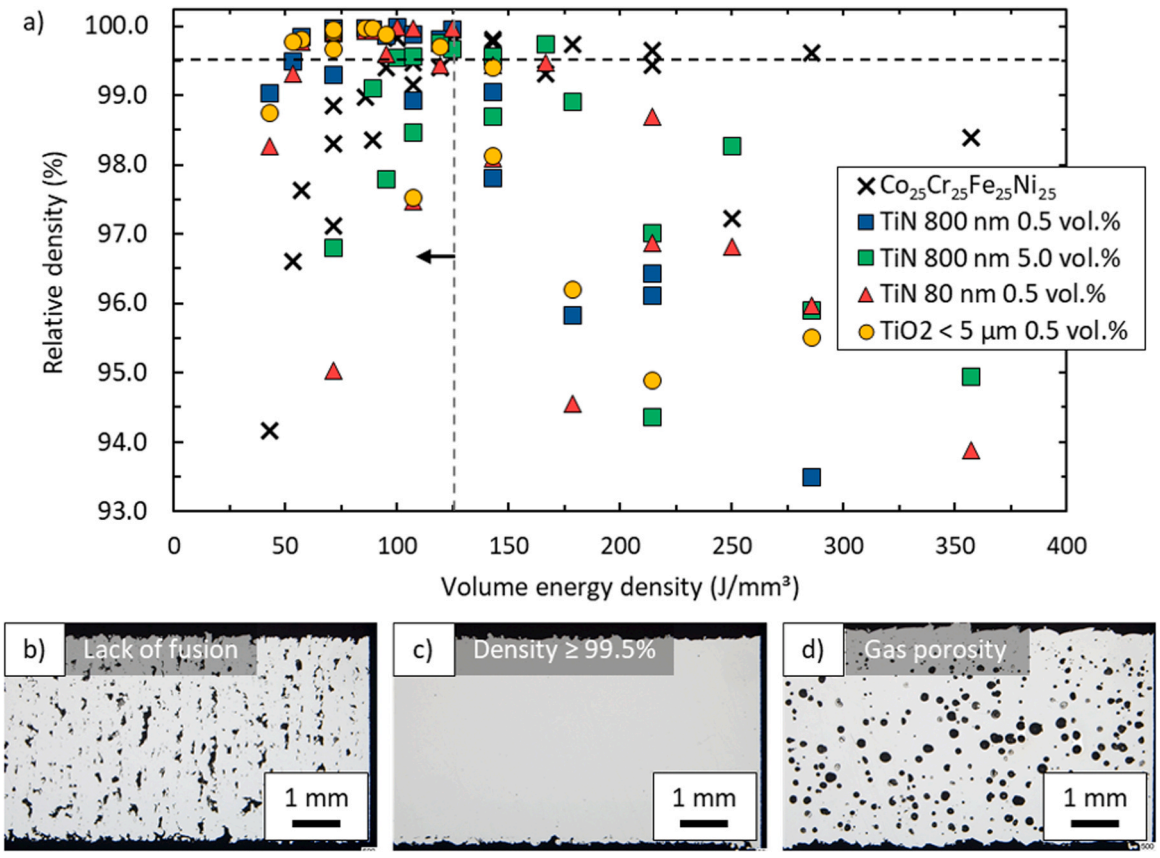

Fig. 2. a) Process evaluation based on optical relative density as a function of volume energy density for the five investigated compositions. Exemplary light optical microscopy images showing b) lack of fusion inherent from comparatively low volume energy density; c) dense sample obtained from relatively intermediate volume energy density; d) increased gas porosity due to relatively high-volume energy density resulting in keyhole formation.

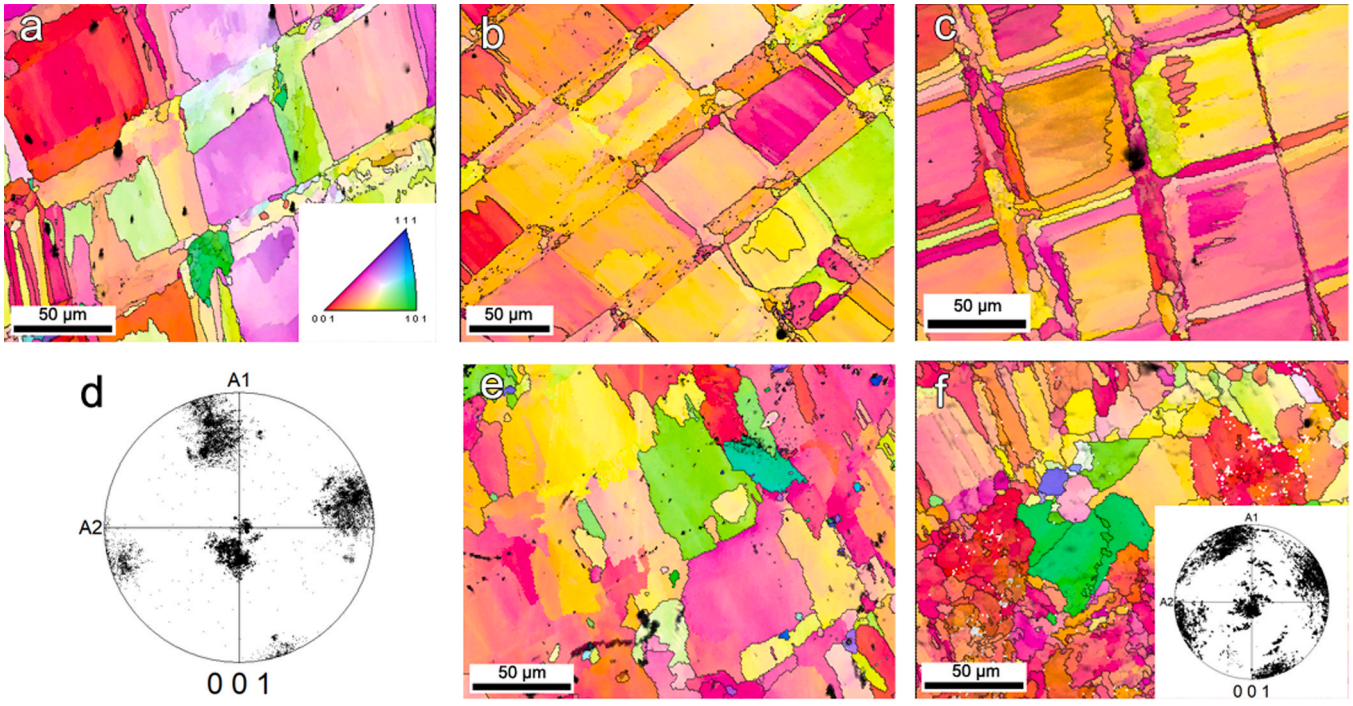

Fig. 3. Inverse pole figure (IPF) orientation maps acquired with out-of-plane build direction using SEM-EBSD from a) the base alloy, and the samples reinforced with b) TiN/0.5/80, c) TiN/0.5/800 with the corresponding pole figure in (d), e) TiN/5/800 and f) TiO_2/0.5/<5000. The printing parameters for all the alloys are provided in Table 1.

bar blanks. The tests were performed according to DIN ISO 6892–1 in air at room temperature on a screw driven machine using an extensometer attaching to the flat gauge section. The test specimens were manufactured vertically so that the loading axis was parallel to the building direction. After machining, the bottom thread was longer compared to the top thread which enabled identification of build direction prior to and post testing.

3. Results

3.1. Microstructure and particle distribution

Fig. 3 shows the inverse pole figure (IPF) orientation maps of all the investigated samples, with the build direction out of plane. The grains are observed to form a checkerboard pattern in the base alloy, and in the TiN particle reinforced alloys (TiN/0.5/80 and TiN/0.5/800). This pattern is created through the laser scan path resulting in a thin band of grains (referred to as 'tracks', hereafter) that are ~70 μm apart, equivalent to the laser scan hatch spacing. The tracks are the region separating the larger square shaped grains (referred to as 'pockets', hereafter). Due to the layer-wise manufacturing process and the rotation angle of 90°, the tracks in one direction appear to be thinner compared to the ones in the perpendicular direction. This effect is due to the cross-section effectively cutting through several tracks at different depth in one plane and has been reported in several alloys [33,34]. For the same reason, the tracks widths seem to differ among samples depicted in Fig. 3. Nevertheless, EBSD analysis of the cross-section in Sup. Fig. 7 shows that the track widths are comparable in TiN/0.5/80 and TiN/0.5/800. An exemplary pole figure of this checkerboard microstructure made up of these tracks and pockets in shown in Fig. 3d. It demonstrates a strong (001) texture. We validated the same on a macroscale using X-ray diffraction (shown in Sup. Fig. 1).

The checkerboard pattern is replaced by a more equiaxed-like microstructure for alloys TiN/5/800 and TiO_2/0.5/<5000. TiN/5/800 displays a large grain size of ~63 ± 7 μm. A bimodal grain size distribution was found for TiO_2/0.5/<5000 with an average size of 31 ± 7 μm for the larger grains and 6 ± 2 μm for the smaller grains. Although the scan direction of the laser can still be estimated from the EBSD in Fig. 3e-f, the pole figure in the inset shows a larger grain orientation spread (also depicted by the x-ray diffraction pole figure in the Sup. Fig. 1).

The STEM-HAADF images in Fig. 4(a, b), reveal that the size range of the reinforcing nanoparticles within all the samples is comparable in the order of 20–100 nm. Despite a tenfold difference in the initial TiN nanoparticle size and the much larger micron sized TiO_2 particles added to the base alloy (see Sup. Fig. 2), all the added nanoparticles converge to similar particle size distribution range. This observation strongly suggests that during the printing process, the nanoparticles melt and dissolve, followed by precipitation, resulting in uniformly sized dispersions. The nanoparticle highlighted in Fig. 4f, confined to a melt pool boundary that was identified using a lower-magnification STEM image, undergoes subsequent remelting during the printing of the next layer. This serves as an additional testament to the melting of the particles under the influence of the applied laser power density. Fig. 4 demonstrates that for all alloys but Ti/5/800, the nanoparticles do not agglomerate, neither in the matrix nor around the melt pool boundaries. Sup. Fig. 2 demonstrates SE-FIB images confirming the even dispersion of nanoparticles observed in both larger and smaller grains across all samples, with Ti/0.5/800 serving as a representative example.

In TiN/5/800, the nanoparticles deviate from the spherical morphology observed in other variants. Typically, nanoparticles with high melting points are anticipated to solidify first, assuming a spherical shape to minimize interface energy. However, in the TiN/5/800 sample, the majority of nanoparticles appear to adopt cubic or cuboidal shapes. Additionally, Fig. 4c also shows a large particle of several microns in the top-left corner. This is formed by several TiN particles fusing together to form TiO_xN_y as we will show in the next section using EDS and EELS analyses on both the particle types.

3.2. Particle structure and chemistry

Fig. 5 presents EDS and EELS data acquired from TiN/0.5/800 and TiN/5/800, respectively. At a low volume percentage (0.5 vol%) addition, TiN undergoes complete oxidation, resulting in negligible nitrogen presence within the particle. Although the printing chamber is flushed with Ar gas, there are trace amounts of oxygen present during the printing process. As Ti has a high affinity for oxygen, it is reasonable to assume that once all of the TiN particles melt and dissolve in the melt pool, TiO_2 precipitates. Furthermore, as seen in Sup. Table 2, the composition of nanoparticles in both TiN/0.5/80 and TiN/0.5/800 was similar. Consequently, given the resemblance in microstructure, nanoparticle composition, and distribution, both samples can be considered as equivalent. EELS data was acquired from the same particles, because the L-edges of transition metals can overlap with the K-edges of oxygen and nitrogen in the EDS spectrum (Sup. Fig. 3).

Fig. 6 shows the elemental maps acquired using EELS from a cuboidal nanoparticle in the TiN/5/800. The maps reveal that the particles have an oxide core and a nitride shell. Such core-shell structures involving oxides of titanium have been observed before [35–37]. Using the EELS quantification method explained in Section 2, we calculated composition profile across the particle. The area scan showed that the shell is stoichiometric TiN and the core is $TiO_{0.6}N_{0.4}$, as seen in Sup. Fig. 4 and Sup. Table 3. However, due to the core being enveloped by the shell, projection-based techniques like EDS or EELS cannot discern the exact composition of the core. The large micron size particle in the bulk is also identified to by an oxynitride using EDS, shown in Sup. Fig. 5.

To further analyze the nanoparticles, we acquired nanobeam diffraction datasets from TiN/0.5/800, TiN/5/800, and TiO_2/0.5/<5000. Selected area diffraction was not feasible for the irregularly shaped shell of the particle; we acquired a 4D-STEM dataset enabling the creation of virtual apertures of any shape as needed. Virtual diffraction patterns obtained from the core and the shell of the nanoparticle are marked in red and orange, respectively (Fig. 7a-c). Both the core and the shell can be indexed as having a cubic crystal structure along the [001] zone axis. Therefore, the core is not tetragonal anatase TiO_2 as observed for TiN/0.5/800 but has a TiO (intermediate oxide) structure, forming an oxynitride. The exact composition was measured using EELS (Sup. Fig. 4).

Fig. 7d-e shows the bright field image and the diffraction pattern obtained from the highlighted green colored virtual aperture obtained from the TiO_2 nanoparticle from the TiO_2/0.5/<5000 sample. The TiO_2 particle was indexed to be in the (111) zone axis of anatase TiO_2. TiO_2 exhibits two polymorphs, rutile and anatase [38]. Despite rutile's thermodynamic stability attributed to its lower free energy, in systems characterized by significant surface area, such as thin films and nanoparticles, anatase exhibits greater stability compared to rutile [39], which explains the presence of anatase nanoparticles in these alloys.

3.3. Nanopores around the particles

Most of the nanoparticles in TiO_2/0.5/<5000 seen in Fig. 4d have tiny pores around them. A closer view of the void can be seen in Fig. 7d and in Sup. Fig. 5. Also, several nanoparticles in both TiN/0.5/800 and TiN/5/800 exhibited similar voids around the particles. In all cases, the pores are randomly located on all sides of the particles, with no relation to the matrix or particle orientation. EELS data was collected and used to create a thickness map, confirming the presence of voids as shown in Fig. 8. As seen in the elemental map, all the elements are depleted in the region that corresponds to a void in the STEM-HAADF image.

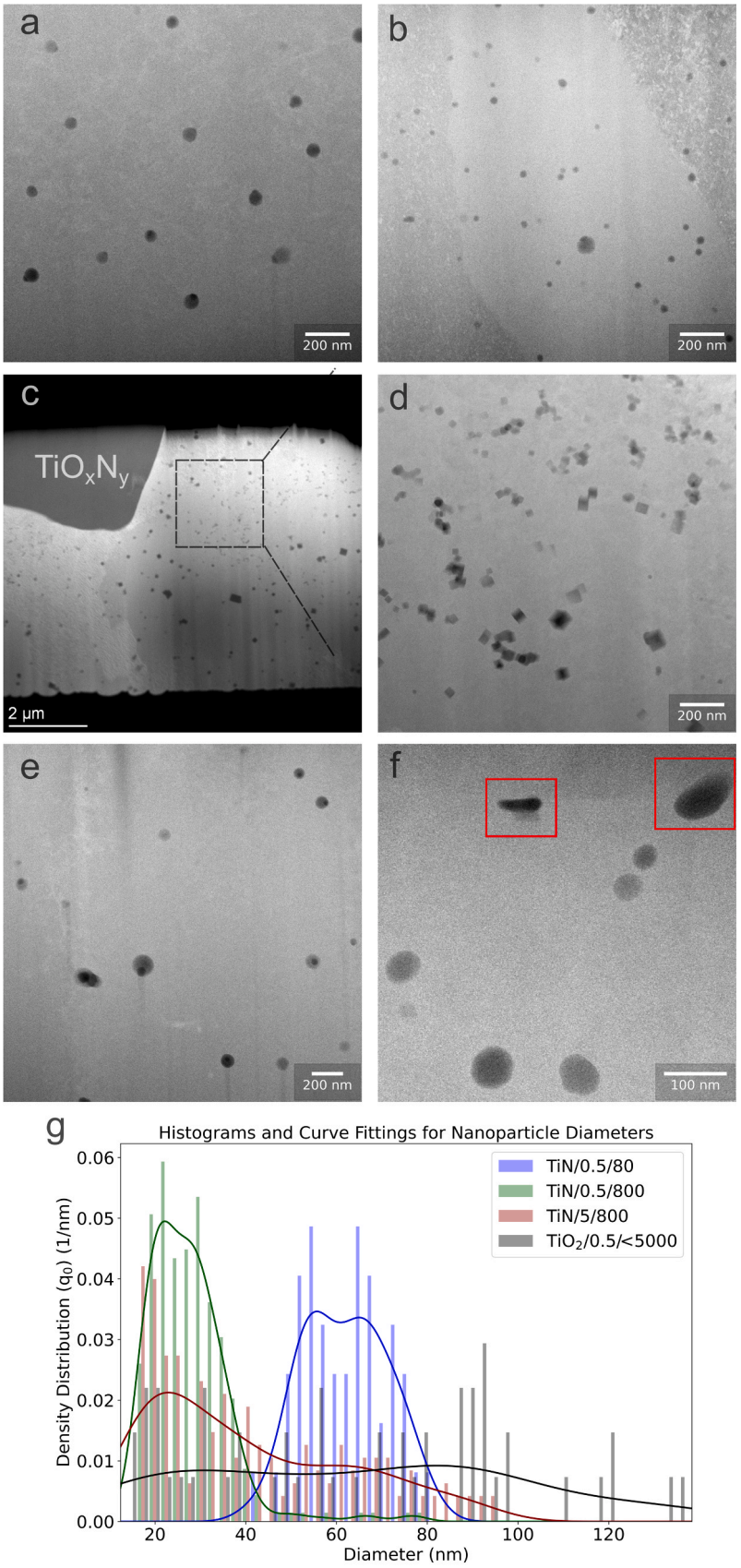

Fig. 4. STEM-HAADF images showing the particle sizes and distribution in a) TiN/0.5/80, b) TiN/0.5/800, c, d) TiN/5/800, e) TiO_2/0.5/<5000. f) HAADF image of nanoparticles in TiN/0.5/800. A partially melted particle in the melt pool boundary is highlighted. g) The histogram shows the particle size distribution in all the samples.

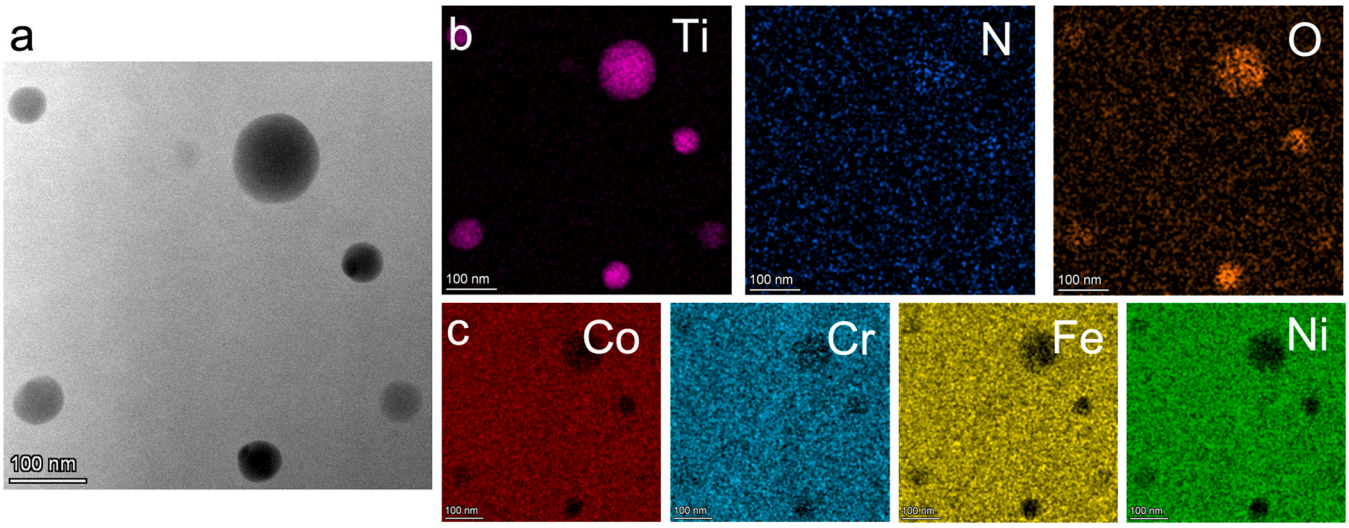

Fig. 5. a) HAADF image of nanoparticle distribution in TiN/0.5/800. b-c) EDS area map of all constituting elements showing O enrichment and N depletion from the nanoparticles. c) The elements in the matrix (Co, Cr, Fe, Ni) are uniformly distributed.

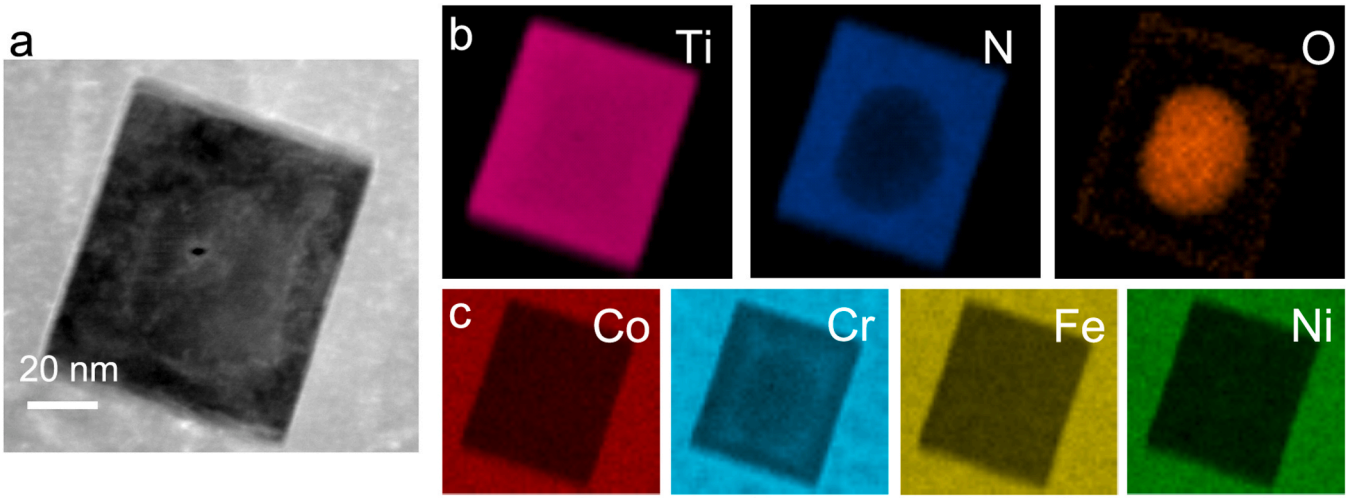

Fig. 6. a) Annular dark field image of a single 'core-shell' structured nanoparticle in TiN/5/800 alloy. b) EELS elemental distribution reveals an oxide core with a nitride shell. c) Uniform distribution of all elements in the matrix.

3.4. Nanoindentation

We utilized nanoindentation to assess the effect of nanoparticle dispersion on mechanical properties. From the mean inter-particle distances obtained from STEM images, we can safely assume a 500 nm deep indent to always interact with several reinforcing particles to give an average representative hardness value. Fig. 9 shows hardness values obtained from the base alloy, TiN/0.5/80, TiN/0.5/800, TiN/5/800 and TiO_2/0.5/<5000. Both TiN and TiO_2 nanoparticles distinctly increase the hardness of the alloy. However, it is the TiN/5/800 sample that exhibits the highest hardness, likely due to a higher fraction of nanoparticles. The remarkable ~40 % increase in hardness observed in the sample containing core-shell nanoparticles compared to the base alloy suggests promising potential for high-temperature applications.

To investigate the observed increase in hardness, we performed STEM imaging of the TiN/0.5/800 alloy before and after nanoindentation. Fig. 9b is an annular bright field (ABF) STEM image, showing a high dislocation density in the as-printed sample, which is a common characteristic of additively manufactured alloys. STEM imaging has proven to be an effective technique for obtaining diffraction contrast from dislocations without the interference of bend contours [40]. To quantify the dislocation contrast (ρ), we utilized the equation $\rho = 2\,n/lt$, where 'n' represents the number of intersections, 'l' is the total length of the grid, and 't' is the thickness of the TEM lamella, estimated to be approximately 100 nm using EELS [41]. To apply this equation, a 10×10 mesh was drawn over the STEM image, and the total number of intersections were counted manually. Using this approach, the dislocation density in the as-printed sample was calculated to be 1.5×10^{14}. In the post-nanoindentation ADF image, as shown in Fig. 9c, a significantly higher dislocation density of 5×10^{14} was observed. This increased dislocation density is expected to result in significant strain hardening. More importantly, the STEM images reveal a strong interaction between the dislocations and the nanoparticles. Dislocations can be observed bending and looping around the particles, which contributes to the observed increase in strength and hardness.

3.5. Tensile testing

In addition to nanoindentation, we carried out tensile tests at room temperature on all five material variants. Fig. 10 shows representative stress/strain curves for the base alloy, TiN/0.5/80, TiN/0.5/800, TiN/5/800 and TiO_2/0.5/<5000. Both TiN and TiO_2 nanoparticles distinctly

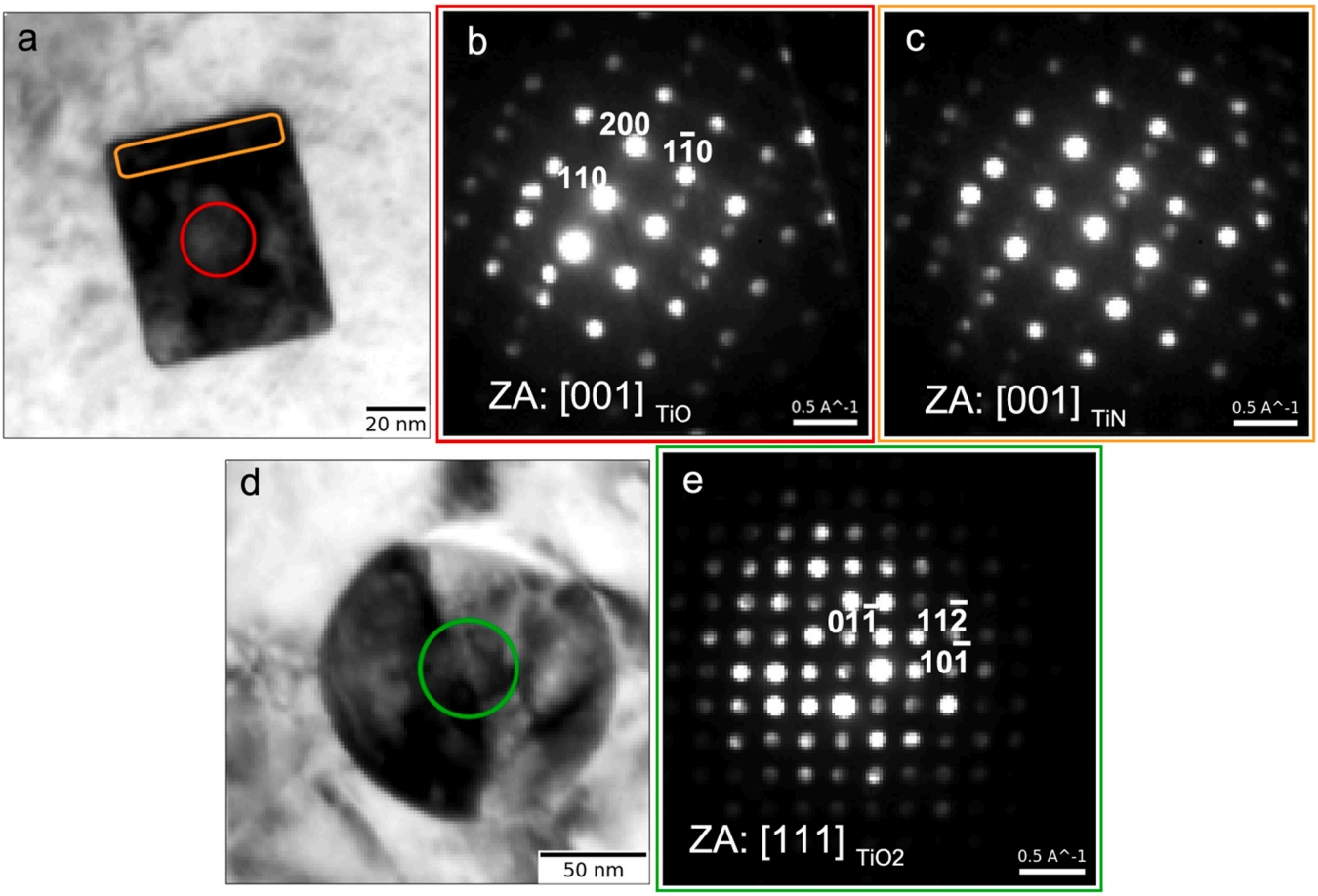

Fig. 7. Nanobeam diffraction from a) core-shell particle in TiN/5/800 with diffraction patterns in b) and c) from the core and shell, respectively. d-e) TiO_2 nanoparticle that is identified as anatase in (111) zone axis.

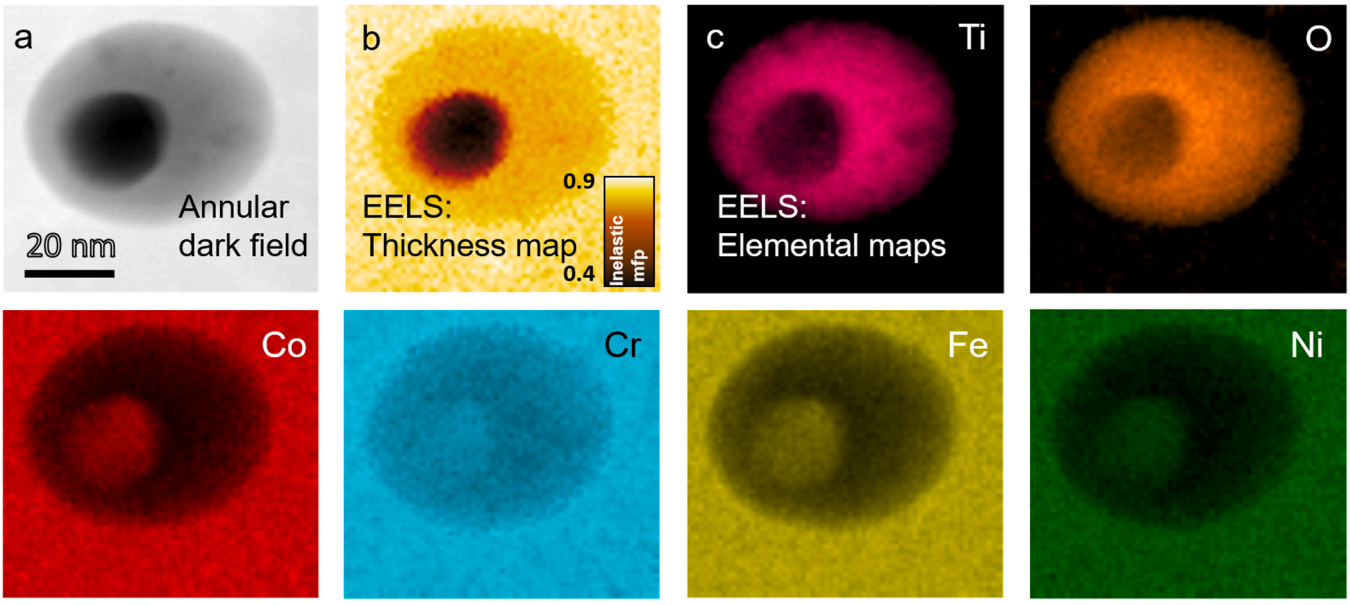

Fig. 8. a) Annular dark field image of a TiO_2 nanoparticle from TiN/0.5/800 sample. b) Thickness map obtained using EELS highlighting the pore in the particle. The color bar represents inelastic mean free path. c) Elemental distribution in the particle and the matrix. The particle is seen to be enriched in Ti and O with a pore in it. Co, Cr, Fe, Ni signal is obtained from the pore, because of additional matrix above or below it.

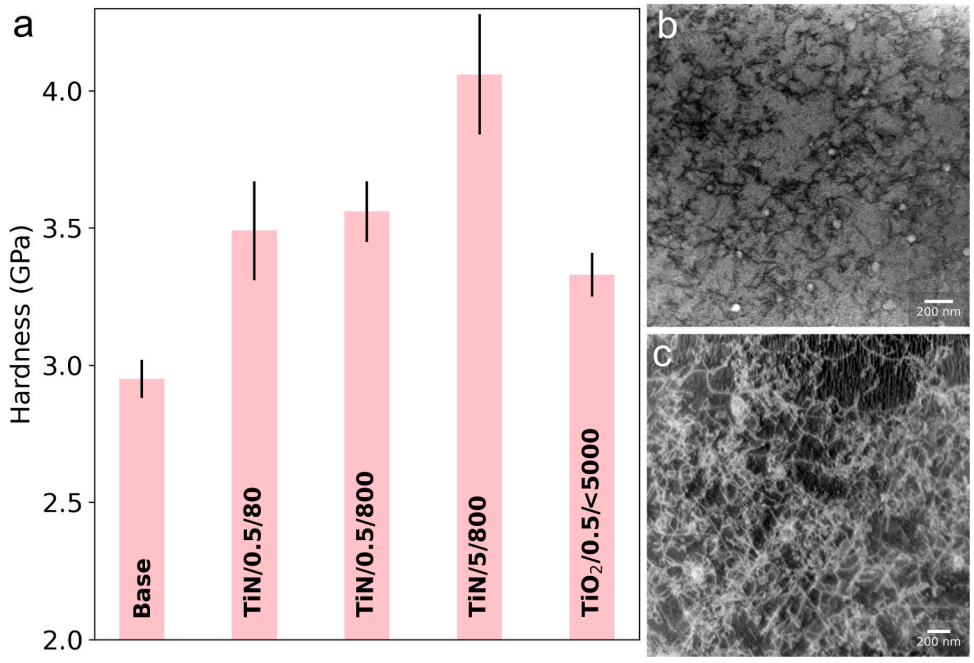

Fig. 9. a) Hardness values obtained from nanoindentation for the base alloy, TiN/0.5/80, TiN/0.5/800, TiN/5/800 and TiO_2/0.5/<5000. The TiN reinforced alloy with the highest volume fraction of initially added nanoparticles demonstrates superior hardness compared to all other alloys. The TiN/0.5/80 and TiN/0.5/800 demonstrate similar hardness owing to similarity in their microstructure and the nanoparticle distribution. The base alloy exhibits the lowest hardness followed by the TiO_2 reinforced counterpart. b) Annular bright field image showing the high density of dislocations in the as-printed TiN/0.5/800 alloy. c) Annular dark field image of a severely deformed region adjacent to the nanoindent, illustrating the strong interaction between the nanoparticles and dislocations.

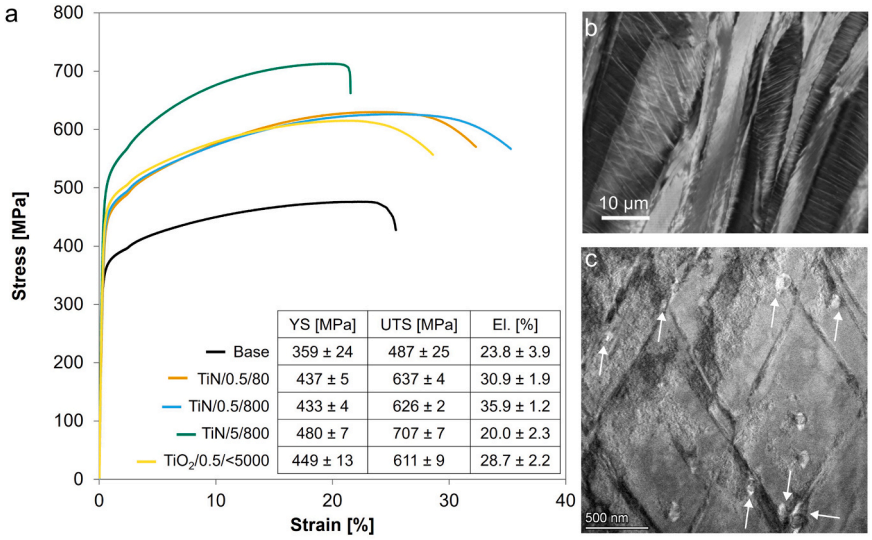

	YS [MPa]	UTS [MPa]	El. [%]
Base	359 ± 24	487 ± 25	23.8 ± 3.9
TiN/0.5/80	437 ± 5	637 ± 4	30.9 ± 1.9
TiN/0.5/800	433 ± 4	626 ± 2	35.9 ± 1.2
TiN/5/800	480 ± 7	707 ± 7	20.0 ± 2.3
TiO_2/0.5/<5000	449 ± 13	611 ± 9	28.7 ± 2.2

Fig. 10. a) Representative stress/strain curves for the base alloy, TiN/0.5/80, TiN/0.5/800, TiN/5/800 and TiO_2/0.5/<5000 loaded uniaxially along the building direction. The table shows the average yield strength (YS), ultimate tensile strength (UTS), and elongation (El.) of four tensile tests at room temperature, respectively. b) FIB-SE image of the cross-section near the fractured surface of the TiN/0.5/800 alloy, showing elongated grains along the tensile axis and extensive twinning. c) Bright-field STEM image taken from a small region in (b), revealing several twin boundaries pinned by particles (marked with white arrows).

increase the strength of the alloy. TiN/5/800 exhibits the highest ultimate tensile strength at 707 MPa which represents an increase of 45 % over the base alloy as well as yield strength with 480 MPa, an increase of 33 %. Small differences can be observed between TiN/0.5/80, TiN/0.5/800, and TiO_2/0.5/<50000, however, all three variants show similar trends compared to the base alloy with increases in ultimate tensile strength between 26 % and 31 % and increases in yield strength between 21 % and 25 %. Detailed analysis of the material close to the fracture surface of one TiN/0.5/800 specimen revealed extensive twin formation across the elongated grains as well as pinning of the twin boundaries at the reinforcing particles (see Fig. 10 b and c).

4. Discussion

4.1. Microstructure

The grains in both tracks and pockets for the base alloy, TiN/0.5/80, and TiN/0.5/800 have a strong (001) texture. This is the most commonly reported texture in LPBF, simply owing to the easy growth direction in the FCC metals. The growth direction follows the direction

of the maximum temperature gradient [34,42,43]. However, scanning parameters and powder characteristics can still largely influence the texture. For example, Geiger et al. were able to tailor the texture between (011) and (001) in the transverse direction by changing the scanning strategy from 0°/90° to ±45° [42]. Similarly, Ishimoto et al. showed a change in texture in the building direction from (011) to (001) when switching the scanning pattern from unidirectional to bi-directional [43]. In a single-directional scan, the (001) orientation forms along the scanning direction. However, in the plane perpendicular to the scan, the orientation depends on the direction of the maximum temperature gradient which is towards the center of the melt pool. This results in (011) texture in building direction. With bi-directional scanning, (001) growth happens along both the x and y axes, which fixes the orientation in the building direction to remain (001). In our study, the bi-directional scanning and the subsequent epitaxial growth lead to the prevalent (001) texture. The presence of other grains in Fig. 3, which exhibit deviations from the (001) texture, is likely attributed to the competing (001) and (011) textures [44,45].

Hu et al. studied influence of printing parameters on texture development in an FCC alloy. They found that when neighboring melt pools overlap less than 50 %, a (011) texture forms with smaller hatch spacing. For larger spacing (>50 μm), a (001) texture is favored [46]. Due to our use of a 70 μm hatch spacing, we observe a predominant (001) texture. With larger hatch spacings, grains within the melt pool tend to grow horizontally instead of at the typical tilt angle (~45°) that favors (011) texture [46].Fig. 11 is an exemplary SEM image that shows the cellular growth of grains in TiN/0.5/800. The lateral growth of the cellular structure in the pockets with respect to tracks is highlighted using cross-section TEM images.

A tenfold increase in the volume fraction of the high melting (3563 K) TiN nanoparticle in TiN/5/800 results in lower peak melt pool temperature because much of the energy is consumed in melting of TiN. As a result, the thermal gradient in the melt pool is lower in TiN/5/800 than in TiN/0.5/800 alloy. The grain size and the texture in LPBF are governed by the temperature gradient (G) and growth rate (R). A change in the G/R ratio from high to low changes the microstructure in the order of planar, cellular, dendritic and equiaxed [47]. An increase of G*R makes the microstructure finer and vice versa [47,48]. An increase in TiN fraction also lowers the thermal conductivity and thereby the cooling rate. Therefore, the reduced G*R leads to coarser grains. Additionally, the unmelted/ partially molten TiN particles are also expected to act as nucleation sites that help to refine the grain size. Overall, the significant increase in added nanoparticle content is likely to change the melt pool dynamics (and temperature) resulting in a more uniform grain size in TiN/5/800.

For TiO_2/0.5/<5000, EBSD (Fig. 3d) indicates a bimodal grain size distribution, with several micron sized grains and a significant fraction of grains > 40 μm. It is expected that TiO_2, due to its low melting point (1843 °C / 2116 K) should melt completely. The larger TiO_2 particles seen the Sup. Fig. 8 that were added to the powder feed may not dissolve completely and may serve as grain refiners, leading to a more equiaxed microstructure compared to the base alloy. Additionally, the (110) texture arises from the use of the same (high) volumetric energy density (Ev) for the low melting TiO_2 as for the high melting TiN. This leads to deeper melt pools as seen in the EBSD from the cross-section in Sup. Fig. 7. The change in the melt pool shape from shallow to key hole-like is likely responsible for the promotion of (110) over (100) texture.

4.2. Nanoparticle size and distribution

The addition of nanoparticles may not only improve the powder flowability and facilitate the printing process [31], but it may also ensure their dissolution in the matrix. This leads to subsequent precipitation as nanoparticles, thereby maintaining small particle sizes and

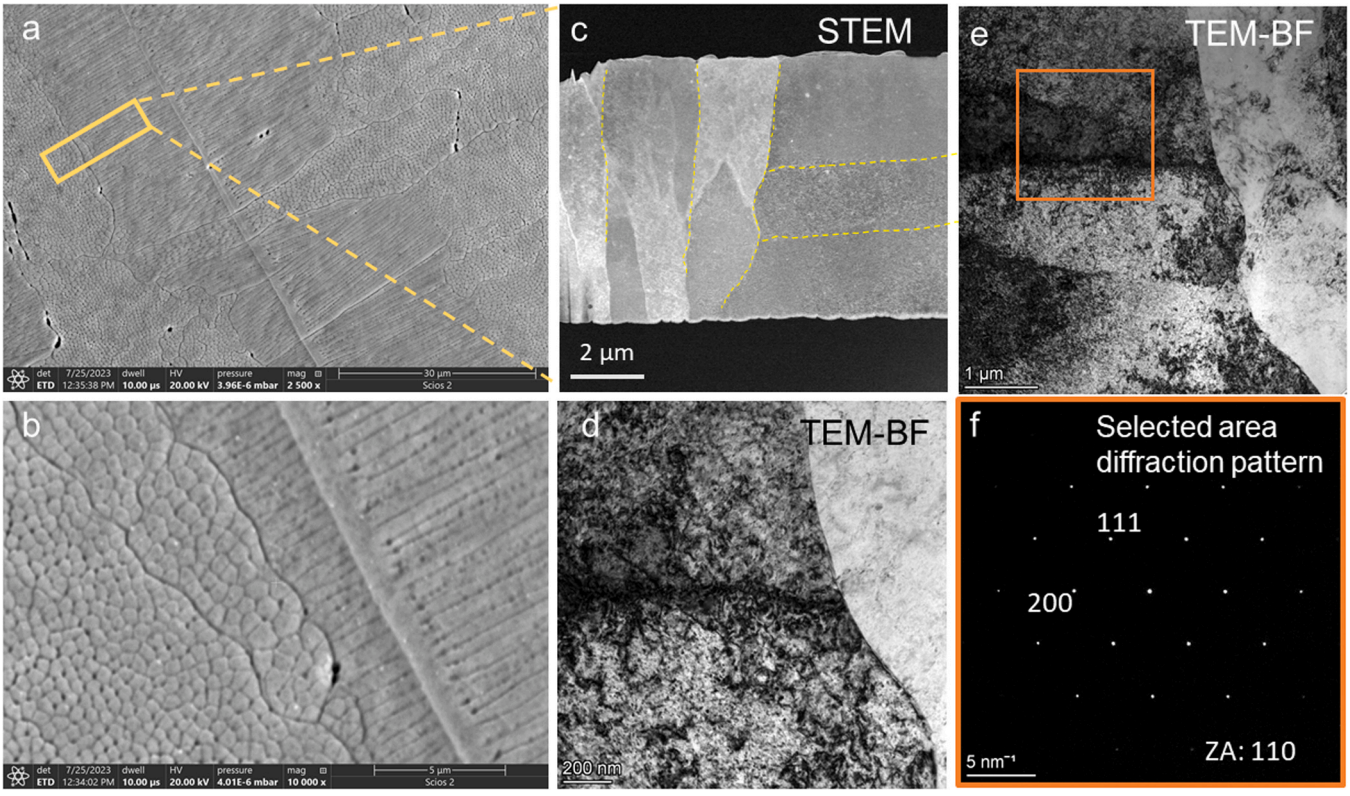

Fig. 11. a-b) Secondary electron image formed using focused ion beam (to obtain channeling contrast) shows the cellular microstructure of the grains in Ti/0.5/800 alloy. The left grain consists of cells that grow upwards against the direction of the heat flow and the right grain consists of cells that grow laterally resulting in (001) texture. c-d) HAADF-STEM and bright field TEM image of TiN/0.5/800 showing the lateral growth of cells from the tracks to the pockets. e-f) Selected area diffraction pattern acquired from the horizontally growing cells marked in orange box, confirming the <100> orientation of their growth.

achieving uniform distribution throughout the material. Du et al. used finite volume method (thermo-capillary convection simulations) to investigate the role of reinforcement particle addition to the convective flow in the melt pool [19]. They showed that by utilizing appropriate volume energy density, homogenous distribution of reinforcements can be obtained. The process is aided by rapid cooling rates and high melt pool temperature, resulting in the Marangoni flow. Subsequently, the molten nanoparticles are thoroughly dispersed in the matrix, as aimed for dispersion strengthened MMC.

Several reports on the homogenous distribution of nanoprecipitates utilizing LPBF have surfaced in recent years [37,49]. In LPBF-ODS steels, the oxide dispersions have most commonly been shown to segregate to the melt pool boundaries or cellular boundaries [26,27]. While the presence of nanoparticles in the cellular boundaries has also been shown to improve the mechanical properties [20,25,29,50], it can be anticipated that trapping the nanoparticles in the interior of the cells should further enhance their strengthening contribution. The interplay of printing parameters and the composition of the powder-particle mix in our study enables the application of a high temperature gradient, such that the rapid solidification front velocity results in nanoparticles that are dispersed within the cells as seen in the TEM images (Fig. 10). The presence of nanoprecipitates both outside and inside the cell walls is anticipated to have resulted in the improved mechanical properties as seen from the nanoindentation and tensile test results.

As seen in Fig. 4, irrespective of the initial TiN size, all nanoparticles dissolve in the melt and precipitate when added in low (0.5) volume percentage. Similarly, AlMangour et al. [51] incorporated TiC in both micro- and nm size to stainless steel that was printed using LPBF. For both initial particle sizes, they found a comparable particle size distribution [51]. The size of particles is primarily determined by the cooling rate and the diffusivity within the melt pool. A reduced cooling rate, which allows for an extended period for diffusion, along with increased diffusivity, facilitates the growth of particles. Recently, in LPBF-based manufacturing of Ni-20Cr ODS alloy (Y_2O_3 nanoparticles), shorter solidification timescales were directly correlated to smaller nanoparticle size and higher number density [52]. Given that all other parameters in the printing process remain unchanged from the base alloy to the nanoparticle-added powders, the melt pool temperature is influenced solely by the nanoparticles that are incorporated. The smaller sized nanoparticles in LPBF produced TiN/0.5/800 (~25 nm) compared to TiN/0.5/80 (~60 nm), as seen in Fig. 4, indicates faster cooling in the former, likely due to the smaller surface area coverage of the metal powder feedstock with nanoparticles in case of 800 nm TiN addition. This enhances the laser-particle interaction that can result in higher peak melt pool temperature. There is also a possibility that the higher melt pool temperature is a result of the lower thermal conductivity of powder bed with 10 times larger nanoparticles. Both cases ultimately lead to smaller sized precipitates. Moreover, varying the initial particle size could potentially enable microstructure tailoring if precipitation behavior differs. However, in cases where similar-sized particles form upon precipitation, employing larger, more cost-effective nanoparticles is a viable strategy.

For TiO_2/0.5/<5000, in Fig. 4g, we see a large spread in the nanoparticle sizes in the printed alloy from 20 to 120 nm. This could be due to a large distribution in the initial particle size of TiO_2 that was mixed in the powder feed from few tens of nm to several microns, as seen in the SEM images in Sup. Fig. 8. The variation in particle size might also result in larger differences in the local TiO_2 concentration and thereby varying temperature field in the region under the laser track and the region further away. It results in TiO_2 particles solidifying at different rates in the tracks and pockets (although the tracks are less clearly visible in TiO_2/0.5/<5000).

4.3. Phase transitions of the particles

For both TiN/0.5/80 and TiN/0.5/800, EDS and EELS revealed the complete oxidation of TiN to TiO_2 that serves as definitive evidence that TiN dissolves and reacts with gases in the melt pool in spite of its exceptionally high melting point of 3220 K. Previous studies have not shown the direct evidence of potential melting behavior of particles of different sizes under similar printing parameters. The processes governing the dissolution of nanoparticles in LPBF are elaborated in [34]. The molten TiN reacts with the oxygen that is gettered from the chamber during the manufacturing. Because the melt pool is enriched with sufficient oxygen for all of the available Ti, there is no residual TiN left. Similarly, Lee et al. added AlN to 316-SS to find that it completely oxidizes to Al_2O_3 [50]. Deng et al. identified comparable oxide inclusions within stainless steel and attributed the oxygen origin to the oxide inclusions in the procured powder and the residual oxygen present in the printing chamber [28]. The potential for cost-effective fabrication of ODS-like alloys, which promise superior high-temperature performance and enhanced radiation resistance, is particularly promising.

For TiN/5/800, while the applied energy density is sufficient in melting the powder feedstock and results in dense material suitable for our investigations, it led to incomplete melting and fusion of several TiN particles forming large micron sized TiO_xN_y (see Sup. Fig. 5). The particles that had melted, precipitated as TiO_xN_y, and were subsequently engulfed with a TiN shell, resulting in a core-shell structure shown in Fig. 5. The quantity of oxygen introduced into the melt pool from the printing chamber is likely insufficient to achieve complete oxidation of the nanoparticles, given the rapid solidification rate, which is exacerbated by the ready availability of N in the melt pool. Because there isn't enough time for the nitrogen to completely degas, it readily forms a nitride shell around the oxynitride. Please note that we examine the crystal structure of the particles once they completely cool down. Therefore, we are oblivious to any solid–state phase transitions that might have occurred during the cooling. The lattice parameters of the cubic TiO and TiN are 4.18 Å [53] and 4.24 Å [54], respectively. The formation of an oxynitride further expands the oxide lattice and reduces the strain. The similarity in the TiO_xN_y and TiN lattice parameters assists in the core-shell formation. Although the lattice parameters cannot be measured with high precision using nanobeam diffraction (due to the finite size of the disks in Fig. 5), the lattice parameters obtained from the diffraction patterns agree well with the literature.

Similar precipitation with increased addition of TiN nanoparticles during LPBF has been also observed by other researchers [36,37]. Zhang et al. added Ti to dual phase steel powder feed saturated with oxygen to form similar core-shell dispersion during LPBF [37]. The TiB_2 nanoparticle addition during CoCrFeNi LPBF fabrication also shows similar core-shell particles [55]. In an Fe-based (Ti, Nb)C composite, it was shown that TiC has a lower Gibbs free energy of formation than NbC that results in a TiC core with a NbC shell around it [56]. The same study also reported that a core-shell precipitate formation leads to increased hardness compared to a single-phase nanoparticle addition. More recently, core-shell precipitate structure was reported in laser-direct energy deposition of $(CoCrNi)_{94}(TiAl)_6$, with an Al_2O_3 core and TiO shell in a CoCrNi matrix that is similar to the present study. The authors also reported a significant improvement in tensile strength [57].

Regardless of whether a boride, carbide, or nitride shell surrounds it, Ti has a significant propensity to produce an oxide core that stems from its strong affinity to oxygen. Nanoparticle growth at higher temperature is a major concern in all alloys and has been often reported in LPBF-based MMCs [58]. The core-shell structure observed in this study is widely known for its effectiveness in preventing nanoparticle coarsening [59–62]. The shell can reduce the interfacial energy or act as a diffusion barrier, hindering capillary-driven coarsening of nanoparticles at high temperatures. This potentially makes Ti an ideal additive in LPBF to form stable nano-dispersions.

4.4. Nanopores

We observed distinct nanopores around several nanoparticles that

were most prominent in TiO_2/0.5/<5000 (Fig. 8, Sup. Fig. 6), but also occasionally present in TiN/0.5/80 and TiN/0.5/800 alloys. As discussed above, due to the lower melting point of TiO_2, the melt pool in TiO_2/0.5/<5000 attains a higher peak temperature. Keyhole formation that is also reflected in the deeper melt pools as indicated by EBSD of its cross-section (Sup. Fig. 7) is likely to result in gas from the chamber getting trapped in the liquid metal. During solidification this gas is entrapped at the particle-matrix interface. Additionally, due to high cooling rates, some of the gas that is released as O_2 and N_2 from the nanoparticles may also get trapped next to them. Li et al. recently showed the nanoparticle dispersion in a FeCrAl alloy [63]. Although not discussed by the authors, their micrographs show similar contrast in the TEM images of their nanoparticles, as seen in the present study. The bright spots around the particles in their BF-STEM images are very likely to correspond to the pores. Although the pores are present around nearly all the particles, they amount to less than 0.15 vol% as analysed using image analysis. Therefore, they have little to no impact on the material density.

More importantly, no pores were observed surrounding any of the core-shell nanoparticles in Ti/5/800. This provides further evidence that pores in the remaining alloys are likely due to residual gases. Additionally, it suggests that incorporating additional Ti may serve as a solution to mitigate undesired pore formation.

4.5. Mechanical behavior

Tensile testing and nanoindentation data reveal that the presence of nanoparticles within the alloy matrix enhance both yield and flow stress response compared to the base alloy. The volume content of nanoparticles appears to be the more significant factor for these effects instead of their type or size distribution. While TiN particles with diameters of 80 and 800 nm displayed slight variations, and TiO2 additions resulted in a broader particle size distribution, these factors exhibited minimal impact on work hardening or the interaction of dislocations and twins with the nanoparticles. Conversely, alterations in particle composition and the formation of core-shell structures appear to exert a more substantial influence on the measured properties. The observed trends in yield and flow stress correlate well with nanoindentation results.

5. Conclusions

In the present work, we used LPBF to print nanoparticle reinforced CCAs. We varied the nanoparticle type, size and the volume fraction systematically to decipher their influence on the microstructure evolution of the alloy.

1. We successfully obtained a densely printed material free of cracks or harmful defects with a uniform dispersion of nanoparticles in the alloy matrix similar to ODS alloys. The nanoparticles were not restricted to cell walls and grain boundaries as commonly reported but present also within the cells.
2. The volume content of 0.5 % TiN melts completely during manufacturing and the titanium gets oxidized to form anatase TiO_2. The microstructure and the resulting mechanical properties are nearly identical for alloys with both 80 nm and 800 nm initial particle addition.
3. Base alloy and the alloys with TiN addition have a cube texture with (001) || building direction due to the 90° scan rotation that encourages epitaxial growth. The texture got weaker with an increase in the volume fraction of the TiN nanoparticle and with the addition of lower melting TiO_2 that encourages (011) || building direction. The addition of TiN in higher volume fraction lowers the temperature gradient in the melt pool, thereby lowering the product of temperature gradient and growth rate (G*R) that aids the equiaxed microstructure.
4. The addition of a larger volume fraction of TiN (5 vol%) results in a core-shell like cuboidal nanoparticles to precipitate that have an oxynitride core and a nitride shell around them.
5. We observed that twin boundaries are pinned by the nanoparticles present in the material. The addition of nanoparticles enhances mechanical behavior mainly as a function of volume content rather than their type or specific particle size distribution. By adding 0.5 vol % of nanoparticles, the ultimate tensile strength increases by about 29 % while adding 5.0 vol% of nanoparticles resulted in a 45 % increase in ultimate tensile strength compared to the base alloy.
6. There is void formation at the interface of particles and matrix that is likely a result of the gas trapped during the solidification. The pores are more prominent in the TiO_2/0.5/<5000 alloy likely due to the keyhole formation during its solidification.

Overall, the CCA microstructure was most significantly affected by the particle type, followed by their volume fraction and size, under constant printing parameters. The uniform dispersion of hard nanoparticles in soft CCA matrix exhibited remarkable improvement in mechanical properties.

CRediT authorship contribution statement

Gerhard Dehm: Writing – review & editing, Supervision, Resources, Funding acquisition, Conceptualization. **Eric A. Jägle:** Writing – review & editing, Supervision, Resources, Project administration, Methodology, Funding acquisition, Conceptualization. **Nils Ellendt:** Writing – review & editing, Supervision, Resources, Methodology, Conceptualization. **Erika Soares Barreto:** Writing – review & editing, Writing – original draft, Visualization, Validation, Methodology, Investigation, Formal analysis, Data curation, Conceptualization. **Fiona Schulz:** Writing – review & editing, Visualization, Validation, Methodology, Investigation, Formal analysis, Data curation, Conceptualization. **Vivek Devulapalli:** Writing – review & editing, Writing – original draft, Visualization, Methodology, Investigation, Formal analysis, Data curation, Conceptualization.

Declaration of Competing Interest

The authors declare that they have no known competing financial interests or personal relationships that could have appeared to influence the work reported in this paper.

Data availability

Data will be made available on request.

Acknowledgment

Authors thank Mr. Benjamin Breitbach for his support with X-ray diffraction measurements. We also thank Dr. Jing Rao for her support with nanoindentation. All authors acknowledge the funding from Deutsche Forschungsgemeinschaft (DFG) – priority program (SPP 2006), Project number 388738622 with projects DE796/13–2, JA2482/3–2 and UH77/11–2.

CRediT statement

V.D.: Conducted formal analysis and investigation, conceptualization and methodology, data analysis, visualization, Writing – original draft, review & editing. **F.S:** conceptualization and methodology, primary investigation, experimentation, Writing – original draft, review & editing. **E.S.B:** procuring raw materials, primary investigation, including data collection, Writing – original draft, review & editing. **N. E.:** developing and planning the experiments, supplied resources, data curation, Writing – review & editing. **E.A.J:** developing and planning

the experiments, supplied resources, Writing – review & editing. **G.D.:** developing and planning the experiments, supplied resources, Writing – review & editing.

Appendix A. Supporting information

Supplementary data associated with this article can be found in the online version at doi:10.1016/j.addma.2024.104338.

References

[1] E.P. George, D. Raabe, Robert O. Ritchie, High-entropy alloys, Nat. Rev. Mater. 4 (2019) 515–534, https://doi.org/10.1038/s41578-019-0121-4.

[2] F.D.C. Garcia Filho, R.O. Ritchie, M.A. Meyers, S.N. Monteiro, Cantor-derived medium-entropy alloys: bridging the gap between traditional metallic and high-entropy alloys, J. Mater. Res. Technol. 17 (2022) 1868–1895, https://doi.org/10.1016/j.jmrt.2022.01.118.

[3] M. Naeem, H. He, S. Harjo, T. Kawasaki, W. Lin, J.-J. Kai, Z. Wu, S. Lan, X.-L. Wang, Temperature-dependent hardening contributions in CrFeCoNi high-entropy alloy, Acta Mater. 221 (2021) 117371, https://doi.org/10.1016/j.actamat.2021.117371.

[4] W. Woo, M. Naeem, J.-S. Jeong, C.-M. Lee, S. Harjo, T. Kawasaki, H. He, X.-L. Wang, Comparison of dislocation density, twin fault probability, and stacking fault energy between CrCoNi and CrCoNiFe medium entropy alloys deformed at 293 and 140K, Mater. Sci. Eng.: A 781 (2020) 139224, https://doi.org/10.1016/j.msea.2020.139224.

[5] Y. Brif, M. Thomas, I. Todd, The use of high-entropy alloys in additive manufacturing, Scr. Mater. 99 (2015) 93–96, https://doi.org/10.1016/j.scriptamat.2014.11.037.

[6] R. Zhou, Y. Liu, C. Zhou, S. Li, W. Wu, M. Song, B. Liu, X. Liang, P.K. Liaw, Microstructures and mechanical properties of C-containing FeCoCrNi high-entropy alloy fabricated by selective laser melting, Intermetallics 94 (2018) 165–171, https://doi.org/10.1016/j.intermet.2018.01.002.

[7] Z. Wu, M. He, H. Cao, S. Wang, R. Chen, B. Cao, R. Shi, X. Liu, S. Yu, S. Wang, J. Bai, J. Wei, Ultrahigh-strength and ductile CoCrFeNi-based high-entropy alloys manufactured by laser powder bed fusion with multiple strengthening mechanisms, J. Mater. Res. Technol. 25 (2023) 2948–2960, https://doi.org/10.1016/j.jmrt.2023.06.110.

[8] N. Ramakrishnan, An analytical study on strengthening of particulate reinforced metal matrix composites, Acta Mater. 44 (1996) 69–77, https://doi.org/10.1016/1359-6454(95)00150-9.

[9] N. Chawla, Y.-L. Shen, Mechanical behavior of particle reinforced metal matrix composites, Adv. Eng. Mater. 3 (2001) 357–370, https://doi.org/10.1002/1527-2648(200106)3:6<357::AID-ADEM357>3.0.CO;2-I.

[10] Y. Yang, J. Lan, X. Li, Study on bulk aluminum matrix nano-composite fabricated by ultrasonic dispersion of nano-sized SiC particles in molten aluminum alloy, Mater. Sci. Eng.: A 380 (2004) 378–383, https://doi.org/10.1016/j.msea.2004.03.073.

[11] S.C. Tjong, Novel nanoparticle-reinforced metal matrix composites with enhanced mechanical properties, Adv. Eng. Mater. 9 (2007) 639–652, https://doi.org/10.1002/adem.200700106.

[12] D. Zhou, F. Qiu, Q. Jiang, Simultaneously increasing the strength and ductility of nano-sized TiN particle reinforced Al–Cu matrix composites, Mater. Sci. Eng.: A 596 (2014) 98–102, https://doi.org/10.1016/j.msea.2013.12.049.

[13] D. Zhou, F. Qiu, H. Wang, Q. Jiang, Manufacture of nano-sized particle-reinforced metal matrix composites: a review, Acta Metall. Sin. 27 (2014) 798–805, https://doi.org/10.1007/s40195-014-0154-z.

[14] J. Hashim, L. Looney, M.S.J. Hashmi, Particle distribution in cast metal matrix composites—Part I, J. Mater. Process. Technol. 123 (2002) 251–257, https://doi.org/10.1016/S0924-0136(02)00098-5.

[15] J. Lan, Y. Yang, X. Li, Microstructure and microhardness of SiC nanoparticles reinforced magnesium composites fabricated by ultrasonic method, Mater. Sci. Eng.: A 386 (2004) 284–290, https://doi.org/10.1016/j.msea.2004.07.024.

[16] W.H. Yu, S.L. Sing, C.K. Chua, C.N. Kuo, X.L. Tian, Particle-reinforced metal matrix nanocomposites fabricated by selective laser melting: a state of the art review, Prog. Mater. Sci. 104 (2019) 330–379, https://doi.org/10.1016/j.pmatsci.2019.04.006.

[17] Y. Zhang, Y. Yu, L. Wang, Y. Li, F. Lin, W. Yan, Dispersion of reinforcing micro-particles in the powder bed fusion additive manufacturing of metal matrix composites, Acta Mater. 235 (2022) 118086, https://doi.org/10.1016/j.actamat.2022.118086.

[18] F. Chang, D. Gu, D. Dai, P. Yuan, Selective laser melting of in-situ Al4SiC4 + SiC hybrid reinforced Al matrix composites: influence of starting SiC particle size, Surf. Coat. Technol. 272 (2015) 15–24, https://doi.org/10.1016/j.surfcoat.2015.04.029.

[19] D. Dai, D. Gu, Influence of thermodynamics within molten pool on migration and distribution state of reinforcement during selective laser melting of AlN/AlSi10Mg composites, Int. J. Mach. Tools Manuf. 100 (2016) 14–24, https://doi.org/10.1016/j.ijmachtools.2015.10.004.

[20] A. Eres-Castellanos, A. Santana, L.M. Sanz-Moral, R. Rementeria, R.H. Pascual, M. Serrano, I. Toda-Caraballo, J.A. Jimenez, F.G. Caballero, C. Capdevila, High temperature performance of 316L steel reinforced by particle inoculation and processed by laser powder bed fusion, J. Mater. Res. Technol. 21 (2022) 2375–2382, https://doi.org/10.1016/j.jmrt.2022.10.053.

[21] N. Kaufmann, M. Imran, T.M. Wischeropp, C. Emmelmann, S. Siddique, F. Walther, Influence of process parameters on the quality of aluminium alloy EN AW 7075 using selective laser melting (SLM), Phys. Procedia 83 (2016) 918–926, https://doi.org/10.1016/j.phpro.2016.08.096.

[22] J.H. Martin, B.D. Yahata, J.M. Hundley, J.A. Mayer, T.A. Schaedler, T.M. Pollock, 3D printing of high-strength aluminium alloys, Nature 549 (2017) 365–369, https://doi.org/10.1038/nature23894.

[23] X.P. Li, G. Ji, Z. Chen, A. Addad, Y. Wu, H.W. Wang, J. Vleugels, J. Van Humbeeck, J.P. Kruth, Selective laser melting of nano-TiB2 decorated AlSi10Mg alloy with high fracture strength and ductility, Acta Mater. 129 (2017) 183–193, https://doi.org/10.1016/j.actamat.2017.02.062.

[24] F. Yan, W. Xiong, E. Faierson, G.B. Olson, Characterization of nano-scale oxides in austenitic stainless steel processed by powder bed fusion, Scr. Mater. 155 (2018) 104–108, https://doi.org/10.1016/j.scriptamat.2018.06.011.

[25] K. Saeidi, L. Kvetková, F. Lofaj, Z. Shen, Austenitic stainless steel strengthened by the in situ formation of oxide nanoinclusions, RSC Adv. 5 (2015) 20747–20750, https://doi.org/10.1039/C4RA16721J.

[26] Y. Zhong, L. Liu, S. Wikman, D. Cui, Z. Shen, Intragranular cellular segregation network structure strengthening 316L stainless steel prepared by selective laser melting, J. Nucl. Mater. 470 (2016) 170–178, https://doi.org/10.1016/j.jnucmat.2015.12.034.

[27] Y.M. Wang, T. Voisin, J.T. McKeown, J. Ye, N.P. Calta, Z. Li, Z. Zeng, Y. Zhang, W. Chen, T.T. Roehling, R.T. Ott, M.K. Santala, P.J. Depond, M.J. Matthews, A. V. Hamza, T. Zhu, Additively manufactured hierarchical stainless steels with high strength and ductility, Nat. Mater. 17 (2018) 63–71, https://doi.org/10.1038/nmat5021.

[28] P. Deng, M. Karadge, R.B. Rebak, V.K. Gupta, B.C. Prorok, X. Lou, The origin and formation of oxygen inclusions in austenitic stainless steels manufactured by laser powder bed fusion, Addit. Manuf. 35 (2020) 101334, https://doi.org/10.1016/j.addma.2020.101334.

[29] N. Chen, G. Ma, W. Zhu, A. Godfrey, Z. Shen, G. Wu, X. Huang, Enhancement of an additive-manufactured austenitic stainless steel by post-manufacture heat-treatment, Mater. Sci. Eng.: A 759 (2019) 65–69, https://doi.org/10.1016/j.msea.2019.04.111.

[30] R. Li, D. Kong, K. He, C. Dong, Superior thermal stability and strength of additively manufactured CoCrFeMnNi high-entropy alloy via NbC decorated sub-micro dislocation cells, Scr. Mater. 230 (2023) 115401, https://doi.org/10.1016/j.scriptamat.2023.115401.

[31] E. Gärtner, A. Witte, N.J. Peter, V. Devulapalli, N. Ellendt, G. Dehm, E.A. Jägle, V. Uhlenwinkel, L. Mädler, Melt pool signatures of TiN nanoparticle dry-coated Co25Cr25Fe25Ni25 metal powder in laser-powder-bed-fusion, Mater. Des. 226 (2023) 111626, https://doi.org/10.1016/j.matdes.2023.111626.

[32] E. Gärtner, H.Y. Jung, N.J. Peter, G. Dehm, E.A. Jägle, V. Uhlenwinkel, L. Mädler, Reducing cohesion of metal powders for additive manufacturing by nanoparticle dry-coating, Powder Technol. 379 (2021) 585–595, https://doi.org/10.1016/j.powtec.2020.10.065.

[33] Y. Tsutsumi, T. Ishimoto, T. Oishi, T. Manaka, P. Chen, M. Ashida, K. Doi, H. Katayama, T. Hanawa, T. Nakano, Crystallographic texture- and grain boundary density-independent improvement of corrosion resistance in austenitic 316L stainless steel fabricated via laser powder bed fusion, Addit. Manuf. 45 (2021) 102066, https://doi.org/10.1016/j.addma.2021.102066.

[34] F.C. Pinto, L.S. Aota, I.R. Souza Filho, D. Raabe, H.R.Z. Sandim, Recrystallization in non-conventional microstructures of 316L stainless steel produced via laser powder-bed fusion: effect of particle coarsening kinetics, J. Mater. Sci. 57 (2022) 9576–9598, https://doi.org/10.1007/s10853-021-06859-1.

[35] J.B. Yoo, H.J. Yoo, H.J. Jung, H.S. Kim, S. Bang, J. Choi, H. Suh, J.-H. Lee, J.-G. Kim, N.H. Hur, Titanium oxynitride microspheres with the rock-salt structure for use as visible-light photocatalysts, J. Mater. Chem. A 4 (2016) 869–876, https://doi.org/10.1039/C5TA06758H.

[36] S.B.A. Malladi, L. Cordova, S. Guo, L. Nyborg, Laser-based Powder Bed Fusion of dispersion strengthened CoCrNi by ex-situ addition of TiN, Procedia CIRP 111 (2022) 368–372, https://doi.org/10.1016/j.procir.2022.08.168.

[37] J. Zhang, H. Dong, X. Xi, H. Tang, X. Li, J.H. Rao, Z. Xiao, Enhanced mechanical performance of duplex stainless steels via dense core-shell nano-inclusions in-situ formed upon selective laser melting, Scr. Mater. 237 (2023) 115711, https://doi.org/10.1016/j.scriptamat.2023.115711.

[38] D.A.H. Hanaor, C.C. Sorrell, Review of the anatase to rutile phase transformation, J. Mater. Sci. 46 (2011) 855–874, https://doi.org/10.1007/s10853-010-5113-0.

[39] H. Zhang, J.F. Banfield, Thermodynamic analysis of phase stability of nanocrystalline titania, J. Mater. Chem. 8 (1998) 2073–2076, https://doi.org/10.1039/A802619J.

[40] P.J. Phillips, M.C. Brandes, M.J. Mills, M. De Graef, Diffraction contrast STEM of dislocations: imaging and simulations, Ultramicroscopy 111 (2011) 1483–1487, https://doi.org/10.1016/j.ultramic.2011.07.001.

[41] Y. Meng, X. Ju, X. Yang, The measurement of the dislocation density using TEM, Mater. Charact. 175 (2021) 111065, https://doi.org/10.1016/j.matchar.2021.111065.

[42] F. Geiger, K. Kunze, T. Etter, Tailoring the texture of IN738LC processed by selective laser melting (SLM) by specific scanning strategies, Mater. Sci. Eng.: A 661 (2016) 240–246, https://doi.org/10.1016/j.msea.2016.03.036.

[43] T. Ishimoto, K. Hagihara, K. Hisamoto, S.-H. Sun, T. Nakano, Crystallographic texture control of beta-type Ti–15Mo–5Zr–3Al alloy by selective laser melting for the development of novel implants with a biocompatible low Young's modulus, Scr. Mater. 132 (2017) 34–38, https://doi.org/10.1016/j.scriptamat.2016.12.038.

[44] M. Higashi, T. Ozaki, Selective laser melting of pure molybdenum: Evolution of defect and crystallographic texture with process parameters, Mater. Des. 191 (2020) 108588, https://doi.org/10.1016/j.matdes.2020.108588.
[45] S.D. Jadhav, S. Dadbakhsh, L. Goossens, J.-P. Kruth, J. Van Humbeeck, K. Vanmeensel, Influence of selective laser melting process parameters on texture evolution in pure copper, J. Mater. Process. Technol. 270 (2019) 47–58, https://doi.org/10.1016/j.jmatprotec.2019.02.022.
[46] Z. Hu, S. Gao, J. Tai, S. Qu, J. Ding, X. Song, Z. Fan, Columnar grain width control for SS316L via hatch spacing manipulation in laser powder bed fusion, Mater. Res. Lett. 11 (2023) 231–238, https://doi.org/10.1080/21663831.2022.2140018.
[47] X. Qi, X. Liang, J. Wang, H. Zhang, X. Wang, Z. Liu, Microstructure tailoring in laser powder bed fusion (L-PBF): strategies, challenges, and future outlooks, J. Alloy. Compd. 970 (2024) 172564, https://doi.org/10.1016/j.jallcom.2023.172564.
[48] Weld Metal Solidification I: Grain Structure, in: Welding Metallurgy, John Wiley & Sons, Ltd, 2002: pp. 170–198. https://doi.org/10.1002/0471434027.ch7.
[49] S. Zhang, K. Li, W. Zhang, M. Ma, M. Li, J. Xue, H. Chen, R. Hu, W. Liu, A novel additive manufactured reduced activation ferritic/martensitic steel enhanced by in-situ nanoparticles benefiting from oxygen addition, Scr. Mater. 235 (2023) 115627, https://doi.org/10.1016/j.scriptamat.2023.115627.
[50] S.H. Lee, S.G. Chung, H.S. Kim, J.-W. Cho, Effects of AlN addition into AISI 316L on melt pool stability and microstructural evolution during laser powder bed fusion, Mater. Sci. Eng.: A 881 (2023) 145311, https://doi.org/10.1016/j.msea.2023.145311.
[51] B. AlMangour, M.-S. Baek, D. Grzesiak, K.-A. Lee, Strengthening of stainless steel by titanium carbide addition and grain refinement during selective laser melting, Mater. Sci. Eng.: A 712 (2018) 812–818, https://doi.org/10.1016/j.msea.2017.11.126.
[52] N.A. Wassermann, Y. Li, A.J. Myers, C.A. Kantzos, T.M. Smith, J.L. Beuth, J. A. Malen, L. Shao, A.J.H. McGaughey, S.P. Narra, Limits of dispersoid size and number density in oxide dispersion strengthened alloys fabricated with powder bed fusion-laser beam, Addit. Manuf. 81 (2024) 104022, https://doi.org/10.1016/j.addma.2024.104022.
[53] M.D. Banus, T.B. Reed, A.J. Strauss, Electrical and magnetic properties of TiO and VO, Phys. Rev. B 5 (1972) 2775–2784, https://doi.org/10.1103/PhysRevB.5.2775.
[54] A. Srivastava, M. Chauhan, R.K. Singh, Pressure induced phase transitions in transition metal nitrides: ab initio study, Phys. Status Solidi (b) 248 (2011) 2793–2800, https://doi.org/10.1002/pssb.201046589.
[55] Y.L. Wang, L. Zhao, D. Wan, S. Guan, K.C. Chan, Additive manufacturing of TiB2-containing CoCrFeMnNi high-entropy alloy matrix composites with high density and enhanced mechanical properties, Mater. Sci. Eng.: A 825 (2021) 141871, https://doi.org/10.1016/j.msea.2021.141871.
[56] C. Zhao, Y. Zhou, X. Xing, S. Liu, X. Ren, Q. Yang, Precipitation stability and micro-property of (Nb, Ti)C carbides in MMC coating, J. Alloy. Compd. 763 (2018) 670–678, https://doi.org/10.1016/j.jallcom.2018.05.318.
[57] X. Bi, R. Li, Z. Yuan, J. Cheng, D. Guan, P. Zhang, Laser-directed energy deposition of a high performance additively manufactured (CoCrNi)94(TiAl)6 medium-entropy alloy with a novel core-shell structured strengthening phase, Addit. Manuf. 80 (2024) 103971, https://doi.org/10.1016/j.addma.2024.103971.
[58] T. Boegelein, S.N. Dryepondt, A. Pandey, K. Dawson, G.J. Tatlock, Mechanical response and deformation mechanisms of ferritic oxide dispersion strengthened steel structures produced by selective laser melting, Acta Mater. 87 (2015) 201–215, https://doi.org/10.1016/j.actamat.2014.12.047.
[59] J.-B. Seol, S.-H. Na, B. Gault, J.-E. Kim, J.-C. Han, C.-G. Park, D. Raabe, Core-shell nanoparticle arrays double the strength of steel, Sci. Rep. 7 (2017) 42547, https://doi.org/10.1038/srep42547.
[60] W. Ding, J. Ma, Y. Jiang, Y. Wang, H. Liu, Developing core-shell nano-structures in FeCrAl-ODS ferritic alloys with the co-addition of Ni and Zr, Acta Metall. Sin. 37 (2024) 364–372, https://doi.org/10.1007/s40195-023-01621-9.
[61] C.S. Bonifacio, S. Carenco, C.H. Wu, S.D. House, H. Bluhm, J.C. Yang, Thermal stability of core–shell nanoparticles: a combined in situ study by XPS and TEM, Chem. Mater. 27 (2015) 6960–6968, https://doi.org/10.1021/acs.chemmater.5b01862.
[62] Y. Wang, S. Zhang, R. Wu, N. Turakhodjaev, L. Hou, J. Zhang, S. Betsofen, Coarsening kinetics and strengthening mechanisms of core-shell nanoscale precipitates in Al-Li-Yb-Er-Sc-Zr alloy, J. Mater. Sci. Technol. 61 (2021) 197–203, https://doi.org/10.1016/j.jmst.2020.05.061.
[63] A. Li, Q. Chen, P. wang, J. Mao, X. Wu, H. Xin, Z. Fang, C. Teng, L. Wu, J. Tang, Laser powder bed fusion of oxide dispersion strengthened FeCrAl alloy: processing and microstructural evolution, Mater. Charact. 208 (2024) 113590, https://doi.org/10.1016/j.matchar.2023.113590.